



Grain Boundary Damage Evolution and SCC Initiation of Cold-Worked Alloy 690 in Simulated PWR Primary Water

Ziqing Zhai, Mychailo Toloczko, Karen Kruska, Daniel Schreiber and Stephen Bruemmer

Abstract Long-term grain boundary (GB) damage evolution and stress corrosion crack initiation in alloy 690 are being investigated by constant load tensile testing in high-temperature, simulated PWR primary water. Six commercial alloy 690 heats are being tested in various cold work conditions loaded at their yield stress. This paper reviews the basic test approach and detailed characterizations performed on selected specimens after an exposure time of ~ 1 year. Intergranular crack nucleation was observed under constant stress in certain highly cold-worked (CW) alloy 690 heats and was found to be associated with the formation of GB cavities. Somewhat surprisingly, the heats most susceptible to cavity formation and crack nucleation were thermally treated materials with most uniform coverage of small GB carbides. Microstructure, % cold work and applied stress comparisons are made among the alloy 690 heats to better understand the factors influencing GB cavity formation and crack initiation.

Keywords Alloy 690 · PWSCC · Creep cavity · Crack initiation · Grain boundary carbide · Cold work · Applied stress

Introduction

Alloy 690 is widely used as a replacement of alloy 600 in pressurized water reactor (PWR) pressure boundary components due to its superior resistance to intergranular stress corrosion cracking (IGSCC). Although no cases of SCC have been reported in this material after more than 25 years in service, laboratory tests [1–6] have shown that cracks in highly cold-worked (CW) alloy 690 can grow in PWR primary water with rates exceeding 10^{-7} mm/s. Based on past experience with alloy 600 that grain boundary (GB) carbides enhance SCC resistance in PWR primary water

Z. Zhai (✉) · M. Toloczko · K. Kruska · D. Schreiber · S. Bruemmer
Pacific Northwest National Laboratory, 622 Horn Rapids Rd,
999, Richland, WA 99352, USA
e-mail: ziqing.zhai@gmail.com

[7, 8], alloy 690 is commonly used in the thermally treated (TT) condition that produces a semi-continuous distribution of GB carbides. However, SCC crack growth tests conducted on alloy 690 at various laboratories [9–11] consistently show a significant reduction in propagation rates in solution-annealed materials as compared to TT materials when tested at the same cold work levels and similar loading conditions. While these results revealed that SCC crack growth susceptibility of alloy 690 increases with cold work and presence of GB carbides, little was known on the effect of cold work and microstructure on SCC initiation behavior. With the increasing interest in extending the life of PWRs worldwide, a better understanding of SCC initiation and the transition to propagation is essential for proactive degradation management. Prior methods to investigate SCC initiation have often used U-bend or reverse U-bend coupons in which the stress distribution is difficult to assess, or slow strain rate tests that significantly accelerate cracking with little relevance to operation conditions. In recent years, compact tension (CT) specimens with a blunt notch or a short pre-crack have been used to evaluate SCC initiation behavior of CW alloy 690 in testing systems equipped with active load control and in situ direct current potential drop (DCPD) monitoring. Arioka et al. [12] detected IGSCC growth from shallow pre-cracks in 20% CW alloy 690TT CT specimens tested at T-L orientation after $\sim 20,000$ h of exposure in 320 and 360 °C PWR primary water. The tests were performed at constant load with initial stress intensity (K) of 23 MPa $\sqrt{\text{m}}$ at 360 °C and 29 MPa $\sqrt{\text{m}}$ at 320 °C. Zhai et al. [13] reported SCC initiation in blunt notch CT specimens from two different 31% CW alloy 690TT heats tested at S-L orientation after $\sim 10,400$ h of exposure in 360 °C PWR primary water. These specimens were subjected to a few gentle loading ramps to 0.5% plastic strain at a slow strain rate of 1×10^{-8} /s during the first 500 h followed by constant K loading at $\sim 36\text{--}37$ MPa $\sqrt{\text{m}}$ for the rest of the test. In both studies, cavities at the interface of GB carbides were observed associated with SCC cracks as well as in the bulk microstructure. Evidence suggested that the cavities can grow under constant load conditions, and that the coalescence of cavities had led to IG crack nucleation. Similar cavity formation was observed in 20% CW alloy 690TT blunt notch specimens in 360 °C creep tests in air and the density increased with applied stress [14]. These observations indicate that creep plays an important role in crack initiation in CW alloy 690 under long-term testing at high stress. However, it is still unclear whether SCC initiation will occur on smooth specimens in PWR primary water under static load conditions. To enable this evaluation, uniaxial constant load tensile (CLT) testing has been conducted on six commercial alloy 690 heats at various cold work levels in a 36-specimen test system. Crack initiation was continuously monitored by in situ DCPD measurements. With carefully planned specimen matrix and test interruptions, accurate parameter control and detailed microstructural characterization, this multi-year test is designed to provide key understanding of SCC initiation mechanisms in CW alloy 690 at conditions more relevant to service practices. The current paper reviews the basic test approach and detailed microscopy characterizations performed on selected specimens after the first test interruption (~ 1 year of exposure) in 360 °C simulated PWR primary water. In the following sections, differences in

the morphology of the precursor damage and cracks will be presented with regard to the cold work level and applied stress for each alloy 690 material. Microstructural comparisons will also be made among heats in order to better understand the factors influencing GB cavity formation and crack initiation in CW alloy 690.

Experimental Procedures

Materials, Specimens and Test Method

Three alloy 690 control rod drive mechanism (CRDM) heats and three plate/bar heats were chosen for SCC initiation testing at various cold work levels achieved by either cold forging or cold rolling. The chemical composition and heat treatment history for each heat is listed in Table 1. Most of the combinations of material and cold work condition had already been evaluated for SCC crack growth behavior as part of a Nuclear Regulatory Commission project at PNNL [15] with results on the influence of cold work on PWSCC crack growth rates summarized in Fig. 1. GB microstructures were characterized for the six heats evaluated in the current study in both the as-received and CW conditions. Carbide precipitation was limited to a few isolated GBs in the mill-annealed (MA) GEG B25 K bar heat, while all the other heats exhibit a semi-continuous GB carbide coverage. However, the size and spacing between carbides vary significantly from heat to heat. As summarized in Table 2, the TT CRDM tubing heats Sumitomo E67074C and Valinox RE243 show the most uniform and closely spaced small carbides, while the TT plate heat TK-VDM 114092 exhibits small carbides at similar size but with a slightly larger spacing. In comparison, the TT CRDM bar heat Doosan 133454 and MA plate heat ANL HK3297HK12 have much larger IG carbides that are more widely spaced. The MA ANL plate heat also features a unique distribution of extensive intra-granular TiN particles. In addition, permanent damage in forms of nano-to-micrometer size cavities and small cracks was found in all CW materials with an example shown in Fig. 2. The density of permanent damage decreased significantly with decreasing cold work level in every heat. A detailed summary on pre-testing microstructural characterizations has been reported elsewhere [16].

SCC initiation behavior is evaluated using the CLT test in an environment that simulates PWR primary water (1000 ppm of boron, 2 ppm of lithium) at 360 °C and 20.4 MPa with a dissolved hydrogen content of 25 cc/kg to maintain a corrosion potential at Ni/NiO stability line. The test was conducted in a 36-specimen test system (Fig. 3a) with three strings that can each accommodate up to 12 actively loaded specimens (Fig. 3b) with in situ DCPD monitoring. The documentation of capabilities for this system and the testing details were described in a previous technical report [17].

Standard 30.4 mm-tall uniaxial tensile specimens were used for this test with dimensions shown in Fig. 3b. All specimens have an identical gauge length of

Table 1 Composition, heat treatment and mechanical properties for the as-received alloy 690TT materials

Source/manufacturer and heat #	Composition, wt%	Heat treatments and room temp. mechanical properties
Valinox/Valinox RE243 CRDM tube	Ni–28.9Cr–10.4Fe–0.02C–0.3Mn–0.35Si–0.14Al–0.23Ti–0.024N–0.008P–0.0005S	1122 °C/~ 1 min, WQ + 716–725 °C/10.5 h, air cool YS = 255 MPa, HV = 157 kgf/mm ²
EPRI/Sumitomo E67074C CRDM tube	Ni–29.8Cr–9.8Fe–0.02C–0.29Mn–0.23Si–0.03Cu–0.0002S	Anneal + 725 °C/10 h/air cool YS and HV not measured
EPRI/TK-VDM (Doosan) 133454 CRDM bar	Ni–29.1Cr–8.9Fe–0.020C–0.26Mn–0.29Si–0.26Al–0.32Ti–0.01Cu–0.02 N–0.005P– <0.002S–0.002B	1045 °C/4 h/WQ + 720 °C/10 h/air cool YS = 263 MPa, HV = 165 kgf/mm ²
ANL/special metals NX3297HK12 plate	Ni–29.5Cr–9.9Fe–0.03C–0.20Mn–0.07Si–0.01Cu–<0.001S	1038 °C/2 h/AC YS not measured, HV = 173 kgf/mm ²
GEG/Allvac B25 K bar	Ni–29.3Cr–9.2Fe–0.034C–0.22Mn–0.06Si–0.26Al–0.37Ti– <0.01Cu–0.03 N–0.006P– <0.0003S– <0.001B	996 °C/20 min/AC YS = 294 MPa, HV = 173 kgf/mm ²
EPRI/TK-VDM 114092 plate	Ni–29.5Cr–9.5Fe–0.020C–0.25Mn–0.26Si–0.32Al–0.36Ti– <0.01Cu–0.003P–<0.002S	1030 °C/1 h/WQ + 715 °C/10 h/AC YS = 285 MPa, HV = 155 kgf/mm ²

Table 2 Summary of grain size and carbide distribution for materials selected for SCC initiation testing at as-received (AR) condition

Material	Grain size (µm)	Carbide location, size	GB carbide density
<i>CRDM materials</i>			
Valinox RE243 TT	~ 90	IG, 50–200 nm	Semi-continuous, spacing ~ 100 nm
Doosan 133454 TT	~ 90	IG, 1–5 µm	Semi-continuous, spacing ~ 0.5–2 µm
Sumitomo E67074C TT	~ 35–40	IG, 50–300 nm	Semi-continuous, spacing ~ 100 nm
<i>Plate/bar materials</i>			
GEG B25 K MA	~ 10–15	TG and isolated IG, 1–3 µm	Low
ANL HK3297HK12 MA	~ 20–25	IG, 0.5–3 µm	Semi-continuous, spacing ~ 0.2–2 µm
TK-VDM 114092 TT	~ 35–40	IG, 50–200 nm	Semi-continuous, spacing ~ 0.1–0.5 µm

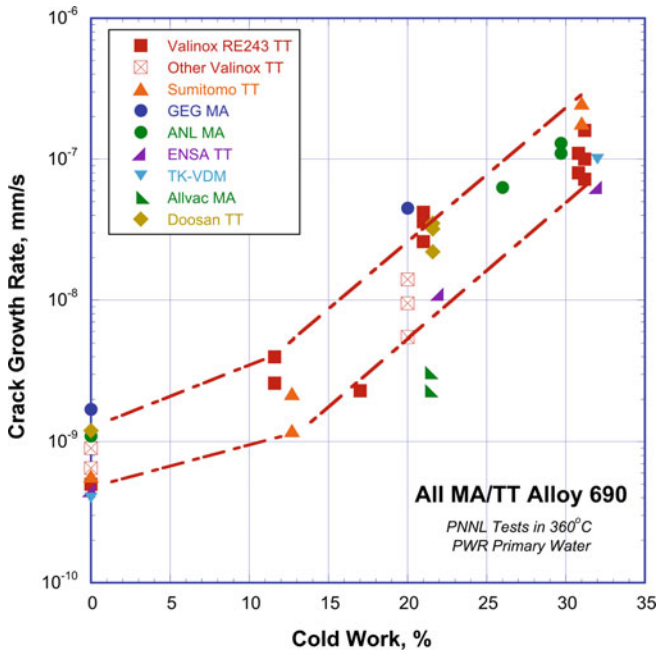


Fig. 1 SCC CGR versus cold work for alloy 690 CRDM, plate and bar heats. Tests were $\sim 30 \text{ MPa}\sqrt{\text{m}}$ at 360°C [15]

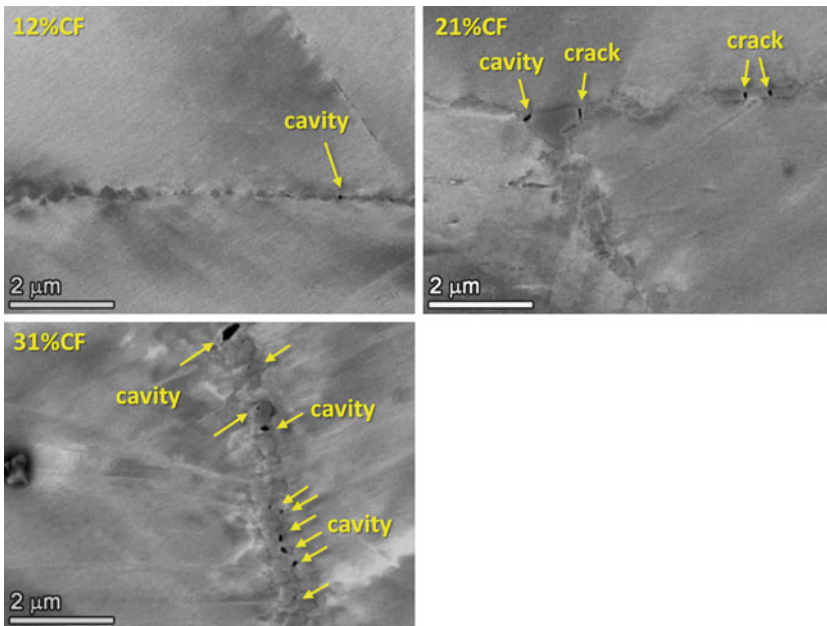


Fig. 2 High magnification SEM-BSE images illustrating the effect of increasing cold work on GB damage in the Valinox CRDM alloy 690TT

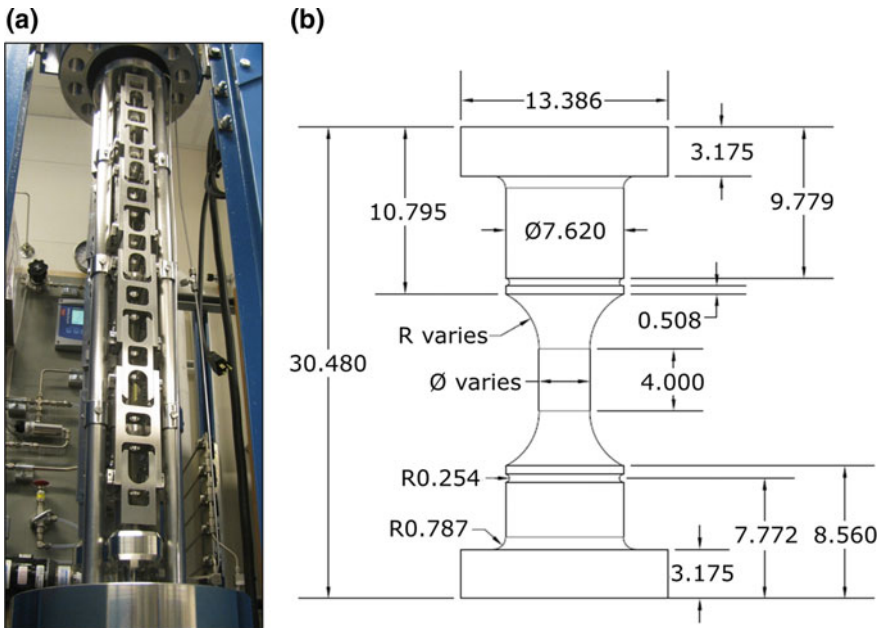


Fig. 3 **a** The 36-specimen SCC initiation testing system and **b** schematic of the dimensions (in mm) of the SCC initiation specimen

4 mm. The relatively small specimen size and gauge length was selected for multi-specimen testing and has the advantage of making DCPD more sensitive to changes in cross sectional area due to cracking. It also enables full characterization of the gauge surface by scanning electron microscopy (SEM) in a reasonable period of time. The specimens were machined with the gauge section along the thickness direction (short transverse) of the forged/rolled block. By varying the diameters of the specimens, different stress levels can be achieved in the specimens in the loading strings to allow them to be tested at their yield stress (or any other target stress) for the applied load.

Testing first began in October 2014 on the 21 alloy 690 specimens identified in Table 3. Materials included two CRDM tubing heats (Sumitomo E67074C and Valinox RE243), one CRDM heat in rod form (Doosan TK-VDM 133464) and one plate heat TK-VDM 114092. All four heats were tested in the TT + 31% and TT + 21% cold-forged (CF) conditions except that the TK-VDM plate heat 114092 was only tested in the TT + 31% CF condition. The applied stress on all specimens was equal to the CW material yield stress (YS). There are three specimens for each combination of heat and cold forge condition, and within each set of three, one has been polished to a 1 μm surface condition, whereas the other two have a rough ground “C” finish on the gauge emulating surface damage condition of in-service LWR components [18]. SCC crack growth testing has been conducted on most of these material conditions with high propagation rates observed for the 31% CF

Table 3 Summary of materials and SCC initiation testing for the 36 alloy 690 specimens

Specimen	Material	Material condition	Surface condition	Applied stress ^a (MPa)	Exposure time (h)
IN024 ^b	Sumitomo CRDM	TT + 21% CF	1 μm	590	9220
IN025	Sumitomo CRDM	TT + 21% CF	Ground C	590	9220
IN026 ^c	Sumitomo CRDM	TT + 21% CF	Ground C	590	9220
IN027 ^b	Valinox CRDM	TT + 21% CF	1 μm	525	9220
IN028	Valinox CRDM	TT + 21% CF	Ground C	525	9220
IN029 ^c	Valinox CRDM	TT + 21% CF	Ground C	525	9220
IN030 ^b	Doosan CRDM	TT + 21.6% CF	1 μm	555	9220
IN031	Doosan CRDM	TT + 21.6% CF	Ground C	555	9220
IN032 ^c	Doosan CRDM	TT + 21.6% CF	Ground C	555	9220
IN033 ^{bc}	Sumitomo CRDM	TT + 31% CF	1 μm	710	9220
IN034 ^c	Sumitomo CRDM	TT + 31% CF	Ground C	710	9220
IN035	Sumitomo CRDM	TT + 31% CF	Ground C	710	9220
IN036 ^b	Valinox CRDM	TT + 31% CF	1 μm	720	9220
IN037	Valinox CRDM	TT + 31% CF	Ground C	720	9220
IN038 ^c	Valinox CRDM	TT + 31% CF	Ground C	720	9220
IN039 ^b	Doosan CRDM	TT + 31% CF	1 μm	685	9220
IN040	Doosan CRDM	TT + 31% CF	Ground C	685	9220
IN041 ^c	Doosan CRDM	TT + 31% CF	Ground C	685	9220
IN042 ^b	TK-VDM plate	TT + 31.9% CF	1 μm	700	9220
IN043	TK-VDM plate	TT + 31.9% CF	Ground C	700	9220
IN044 ^c	TK-VDM plate	TT + 31.9% CF	Ground C	700	9220
IN053 ^b	ANL flat bar	MA + 26% CR	1 μm	775	7110
IN054	ANL flat bar	MA + 26% CR	1 μm	775	7110
IN055 ^c	ANL flat bar	MA + 26% CR	Ground C	775	7110
IN056 ^b	GE B25 K bar	MA + 18.3% CF	1 μm	550	7110
IN057	GE B25 K bar	MA + 18.3% CF	1 μm	550	7110
IN058 ^c	GE B25 K bar	MA + 18.3% CF	Ground C	550	7110
IN059 ^b	TK-VDM plate	TT + 21% CR	1 μm	675	7110
IN060	TK-VDM plate	TT + 21% CR	1 μm	675	7110
IN061 ^c	TK-VDM plate	TT + 21% CR	Ground C	675	7110
IN062 ^b	GE B25 K bar	MA + 12.4% CF	1 μm	510	7110
IN063	GE B25 K bar	MA + 12.4% CF	1 μm	510	7110
IN064 ^c	GE B25 K bar	MA + 12.4% CF	Ground C	510	7110
IN065 ^b	Valinox CRDM	TT + 11.7% CF	1 μm	365	7110
IN066	Valinox CRDM	TT + 11.7% CF	1 μm	365	7110
IN067 ^c	Valinox CRDM	TT + 11.7% CF	Ground C	365	7110

^aThe applied stress is the yield stress of the specimens at the tested temperature (360 °C)

^bSpecimens instrumented by DCPD and observed for gauge surface

^cSpecimens observed for cross-section

Sumitomo and Valinox materials and moderate propagation rates for all three CRDM heats in the 21% CF condition as shown in Fig. 1.

After ~ 2100 h of operation, 15 additional CW alloy 690 specimens were inserted. These include specimens from the ANL (Special Metals) flat bar heat NX3297HK-12 in the mill-annealed (MA) + 26% cold-rolled (CR) condition, the GEG (Allvac) bar heat B25 K in the MA + 18% CF and MA + 12% CF conditions, the TK-VDM 114092 plate in the TT + 21% CF condition, and the Valinox CRDM heat RE243 in the TT + 12% CF condition. Only the 26% CR ANL and 12% CF Valinox materials have been evaluated for SCC crack growth. The ANL material exhibited high propagation rates, while the Valinox material exhibited limited IG engagement and low SCC growth rates during testing (Fig. 1). The B25 K and TK-VDM heats were not examined in these CF conditions, however they did show moderate SCC growth rates with higher levels of cold work. Three specimens were again prepared for each combination of heat and cold work condition, but this time two of them are with 1 μm finish while the other one is at ground "C" finish. Summary information on the 15 additional alloy 690 specimens is also given in Table 3. Testing was restarted with all 36 specimens again loaded to their yield stress until the total exposure time reached 9220 h (~ 1.1 year) for the first 21 specimens and 7107 h (~ 0.8 year) for the other 15 specimens. The test was then stopped and SEM characterization was carried out with the original purpose of recording precursor damage on the surface of highly polished specimens before returning them for continued exposure.

Microstructural Characterizations

Scanning Electron Microscopy and Focused Ion Beam Examinations

Microstructural examinations were conducted using a JEOL 7600 scanning electron microscope and an FEI Quanta field emission gun focused ion beam (FIB) system. Characterizations started by documenting the entire gauge surface using SEM of the 12 instrumented, highly polished specimens as identified in Table 3. In order to achieve this, four fiducial scribe marks (90° to one another) were made at the button ends of each specimen to keep track of the specimen orientation. Each of the four orientations was then mapped using high-kV backscatter electron (BSE) montage imaging so that features covered by thin surface oxides can be revealed. In order to better characterize surface and near-surface SCC precursors, FIB was employed to create shallow trenches to investigate selected features in cross-section. By milling off a certain amount of material slice by slice in the area of interest, damage features could be imaged in 3D enabling spatial characteristics to be determined. Details of this technique and its application to these specimens are presented elsewhere [19].

As will be shown in the next section, SEM surface examination and serial FIB milling revealed GB cavities as precursors to IG oxidation and crack initiation. This evoked a high interest of a thorough examination on GB cavity distribution in the

bulk materials. Since the rough surface of the ground samples made it very difficult to identify cracks on the gauge surface, the decision was made to discontinue testing and cross-section selected ground specimens. A total of 13 specimens as marked in Table 3 were removed including one ground specimen from every combination of heat and cold work condition, as well as the 1 μm finish 31% CF Sumitomo CRDM specimen IN033 that showed the most extensive IG cracks on the gauge surface. These specimens were sectioned in half along the axial direction and the two halves were polished to a colloidal silica finish. High-kV BSE montage imaging was first performed on the entire gauge cross-sections followed by low kV, higher resolution imaging at a number of sites that appear to contain GB cavities based on indications from the montage images. Observations were also made near the mid position of the specimen gauge to evaluate cavity morphology and density as a function of distance from the surface through the entire specimen thickness by examining regions that were ~ 0.5 mm apart.

Quantification of GB Cavity Distribution

While the approach described above would provide qualitative information on the precursor damage and cracks, systematic quantification were also conducted in order to better understand the evolution of GB cavities with a focus on the effect of starting microstructure and applied stress. Prior to the SEM examination, finite element modeling (FEM) was performed to analyze the stress distribution in selected specimens from the gauge mid-position to the fillet region where a gradually increasing diameter results in decreased stress, and the locations corresponding to an applied stress of 85, 70, 50 and 15% of the YS were identified. The quantification first started on the cross-section of one of the ground, 31% CF specimens from the Valinox and Doosan CRDM heats that exhibited different GB carbide morphologies noted in Table 2. As shown in Fig. 4, an area with a fixed size of $150 \times 150 \mu\text{m}$ near the centerline was selected at each location based on low-magnification montage image where a high density of GB cavities were indicated. The size of the squared area was chosen such that a minimum of 3–4 grains can be included irrespective of heat. Higher magnification BSE images were taken along every high-energy GB included in the area. A magnification of 15,000X was chosen to allow cavities with a size down to 2 nm to be sufficiently resolved. The contrast and brightness were fixed during imaging in order to prevent any unwanted bias in cavity size due to change in image settings. Generally, 100–150 images were taken at each area, stitched together and processed in the image processing program *ImageJ*. While most of the unwanted background signal was removed by the software, further correction was manually made on erroneous features by comparing the processed images to the original ones. These mainly include unremoved TiN precipitates and surface contamination due to contrast similar to that of the cavities, as well as partially missing cavities due to accumulation of polish remnants inside cavities that are not identified by *ImageJ*. An example of the process is provided in Fig. 5. The final outcome is shown in Fig. 5c

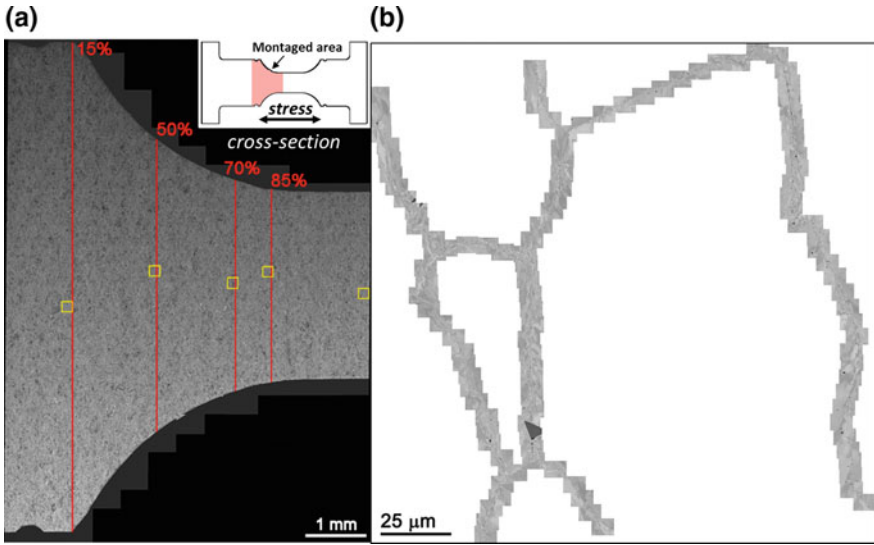


Fig. 4 a SEM-BSE montage image of the fillet and part of the gauge region in TT + 31% CF Doosan CRDM specimen IN041 with locations corresponding to 15, 50, 70 and 85% applied stress (YS) marked with red lines. The $150 \times 150 \mu\text{m}$ area selected for cavity quantification at each location is highlighted in yellow. b Stitched high-magnification SEM-BSE images showing the GBs documented for cavity quantification at the area corresponding to 70% YS in IN041 (Color figure online)

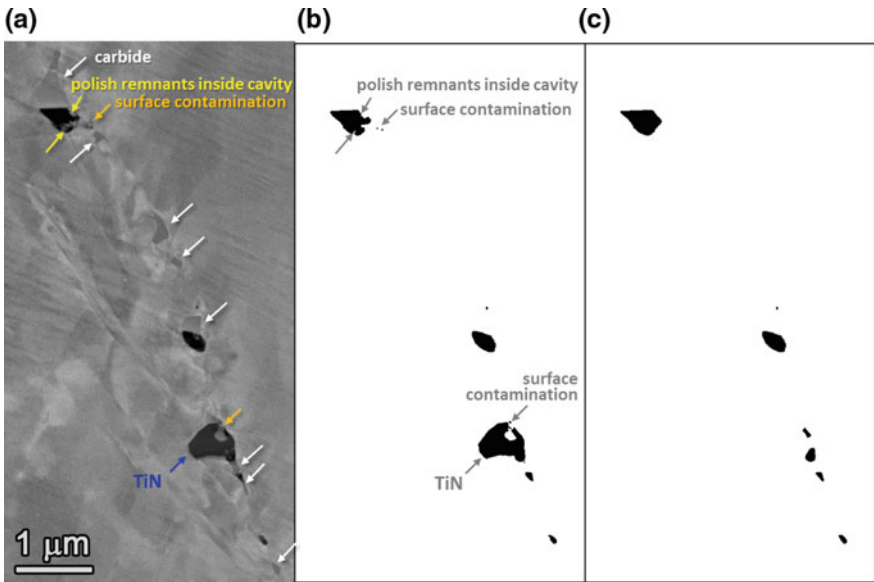


Fig. 5 Image processing steps for cavity quantification: a original SEM-BSE image showing cavities, carbides and a TiN particle on a GB. SEM-BSE image processed using a routine created in *ImageJ* in (b) with almost everything removed except the GB cavities and the TiN particle. c Manual adjustments are made to the processed image in (b) to isolate GB cavities with their correct shapes shown in image (a)

where all the background is removed, leaving only the GB cavities with the exact shape as those in the original image. Upon completion of image processing on the GBs, data on the number and size of the cavities were collected using *ImageJ* automatically.

Results

DCPD Measurements

Due to space limitations within the autoclave, only one (with 1 μm finish) out of each set of 3 duplicate CLT specimens could be instrumented for DCPD. The DCPD signal is sensitive not only to cracking but also to changes in length and diameter due to creep or tensile straining, as well as to resistivity changes that occur in alloy 690 when exposed at PWR relevant temperatures. In this test, DCPD values are presented as strain measurements because up to the point of significant crack formation, creep deformation is believed to more strongly affect the DCPD signal than cracking. However, it should be noted that resistivity changes affect the DCPD signal (particularly early in the test) and create a higher strain rate than due to creep alone. An example of the DCPD-based strain response of the instrumented 21 and 31% CF Sumitomo and Valinox CRDM specimens during the latest 6220 h of testing is presented in Fig. 6. Slightly higher strain rates can be seen for the 31% CF

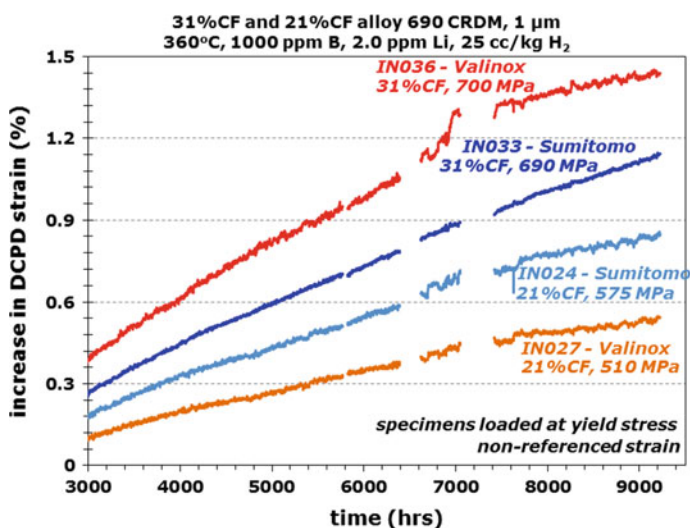


Fig. 6 DCPD non-referenced strain response for the 21 and 31% CF specimens from Sumitomo and Valinox CRDM heats from ~ 3000 to ~ 9220 h (time of the test interruption) of exposure

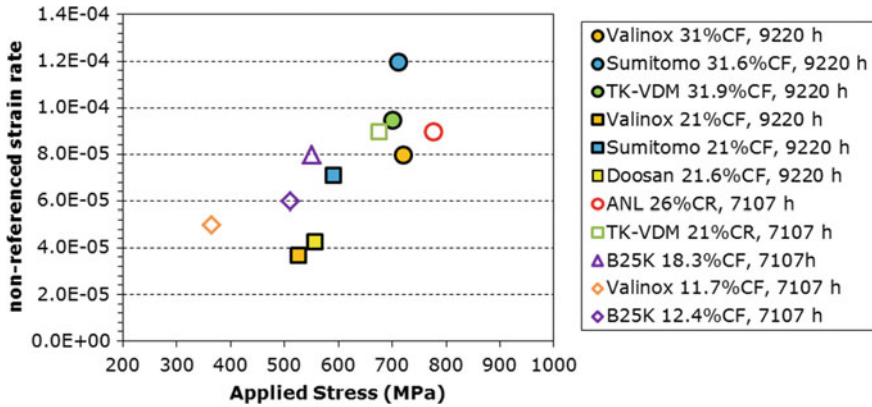


Fig. 7 DCPD non-referenced strain rate over the latest ~ 2500 h as a function of applied stress in the tested alloy 690 CLT initiation specimens

specimens than for the lower CW materials. The other specimens have a similar trend in responses. This can be viewed more clearly in Fig. 7 where the DCPD-indicated non-referenced strain rate over the last 2500 h is plotted against applied stress. The increase in strain rates tends to scale with applied stress likely due to the contribution of creep. Meanwhile, there is also a continually decreasing trend over time in the strain rate response of all the specimens due to an exhaustion of primary stage creep and a slowing resistivity evolution since material changes saturate after long exposures at 360 °C.

Gauge Surface Examination of GB Damage

Precursor Damage and Crack Morphology on the Surface of the Polished Specimens

As mentioned in Sect. 2.2.1, SEM characterizations started by documenting the entire gauge surface of the 12 instrumented, highly polished specimens marked in Table 3. Figure 8 shows the typical appearance of the gauge surface on a randomly selected rotation of the four examined 31% CF specimens. Obvious cracks are highlighted in red and possible cracks are highlighted in green whenever they can be readily identified on the surface. The obvious cracks usually appear open or partially open with a surface length greater than ~ 10 μm , whereas the possible cracks feature continuous dark contrast along GBs with a similar or longer length without a detectable opening. Somewhat unexpectedly, multiple IG cracks were easily identified on three of these specimens with the highest density in the 31% CF

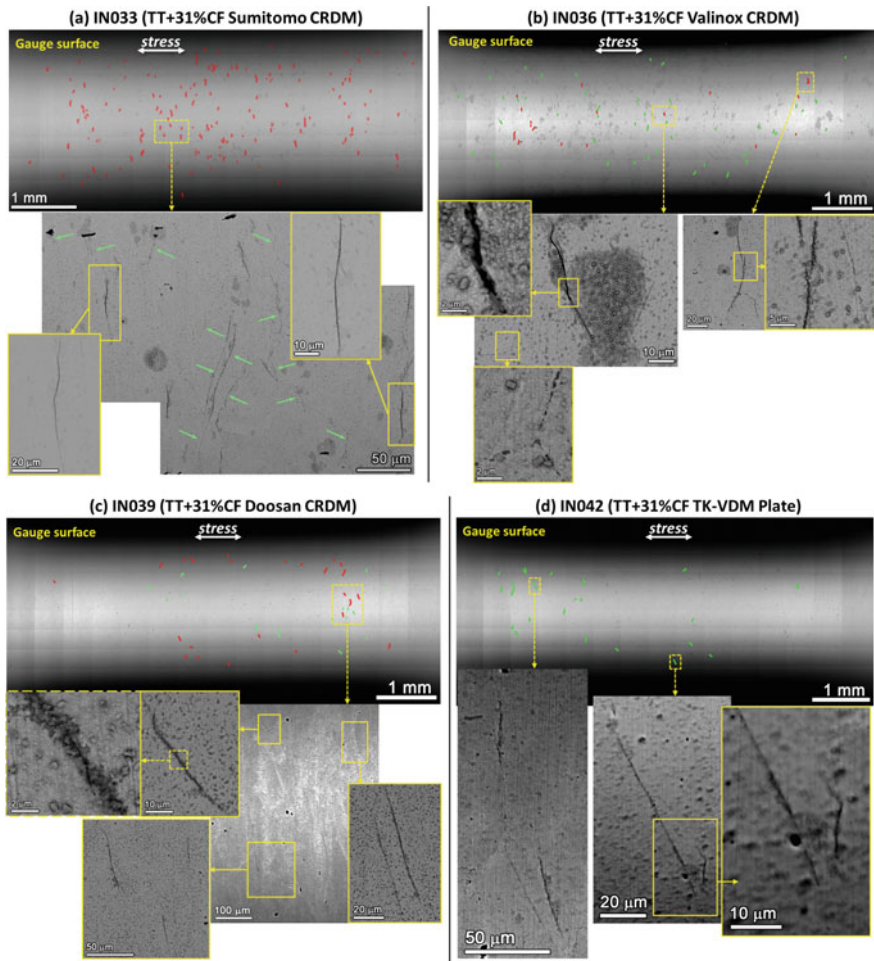


Fig. 8 SEM-BSE montage images (upper) and higher magnification SEM-BSE images (lower) on precursor damage on the gauge surface in one rotation of the 1 μ m finish, 31% CF specimens **a** IN033 (Sumitomo CRDM), **b** IN036 (Valinox CRDM), **c** IN039 (Doosan CRDM), and **d** IN042 (TK-VDM plate) after 9220 h of exposure. Obvious cracks are highlighted in red and possible cracks are highlighted in green. Possible cracks are not highlighted in the upper low-resolution montage image in **(a)** because of their extremely high density in this specimen (Color figure online)

Sumitomo CRDM specimen IN033 (Fig. 8a), followed by the 31% CF Valinox CRDM specimen IN036 (Fig. 8b) and the 31% CF Doosan CRDM specimen IN039 (Fig. 8c) in a decreasing order. The 31.9% CF TK-VDM specimen IN042 did not show any obvious cracks but some features indicative of possible cracks were found (Fig. 8d). The specimen with the next highest CW level is the

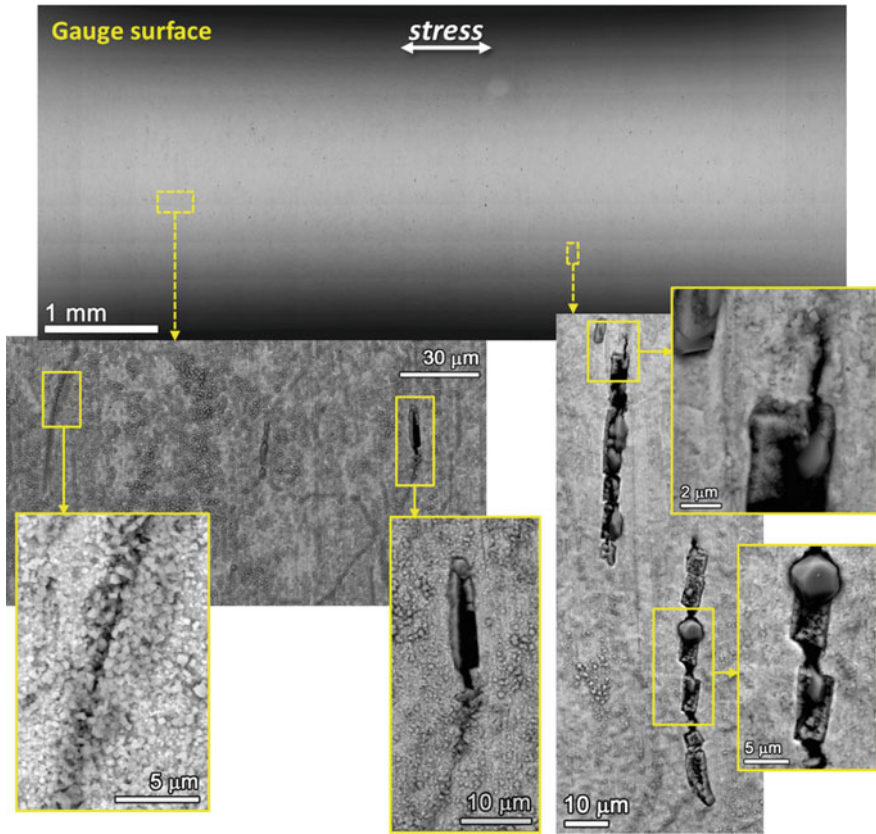


Fig. 9 SEM-BSE montage images (upper) and higher magnification SEM-BSE images (lower) on precursor damage on the gauge surface in one rotation of the 1 μm finish, 26% CR ANL plate specimen IN053 after 7107 h of exposure

26% CR ANL plate specimen IN053. This specimen exhibited a distinctively different surface morphology with extensive transgranular (TG) TiN second phase particles that were favored sites for crack nucleation (Fig. 9). These TiN particles commonly present in stringers and were often cracked due to initial cold rolling. The higher-magnification images in the lower right of Fig. 9 reveal additional cracking and corrosion formed at cracked TiN particles. However, previous SCC initiation testing and microstructural characterizations indicated that the cracks associated with these TiN particles had remained shallow (a few micrometers) even after aggressive loading and an exposure time of $\sim 10,000$ h [17].

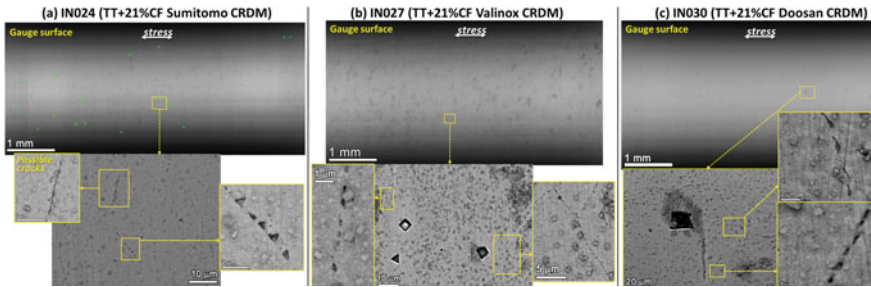


Fig. 10 SEM-BSE montage images (upper) and higher magnification SEM-BSE images (lower) on precursor damage on the gauge surface in one rotation of the 1 μm finish, 21% CF specimens **a** IN024 (Sumitomo CRDM), **b** IN027 (Valinox CRDM), and **c** IN030 (Doosan CRDM) after 9220 h of exposure

A significant decrease in crack density was observed for the specimens at cold work levels of 21% or less. As shown in Fig. 10, the highly polished 21% CF specimens from the three CRDM heats did not exhibit any obvious IG cracks. However, many high-energy GBs in these specimens exhibit a “postage stamp” appearance with semi-continuous distribution of small, dark holes. Similar features were also commonly found along uncracked high-energy GBs in the highly polished 31% CF specimens as evidenced in Fig. 8b. The rest of the specimens showed little or no identifiable IG damage on the surface thus the images are not presented in this paper but can be found elsewhere [16].

FIB Examination on Selected Polished Specimens

To gain more information on the surface cracks, FIB was employed to trench below the surface of the 31% CF Sumitomo CRDM specimen IN033 and the 31% CF Valinox specimen IN036 to examine the cracks in profile. This has been proved as an efficient and non-destructive characterization method for specimens that can be returned to testing [17]. Trenches were first made to intersect IG cracks with various surface lengths in these two specimens to check the depth of these cracks. Quite surprisingly, results shown in Fig. 11 revealed that many IG cracks had already exceeded 15 μm in depth (beyond the depth of the FIB trenches) at locations relatively far from the widest opening portion of the crack shown on the surface where the depth is expected to be even deeper. Another finding is that nano-sized GB cavities were often present along the walls of these deep cracks, whereas shallower and tighter cracks always ended at GBs containing a distribution of cavities.

In addition, serial FIB milling was conducted on the 21% CF Sumitomo CRDM specimen IN024 to investigate subsurface morphology of the GBs showing the “postage stamp” appearance. As shown in Fig. 12, the nano-sized holes observed on the surface were always linked to a continuous distribution of sub-surface IG

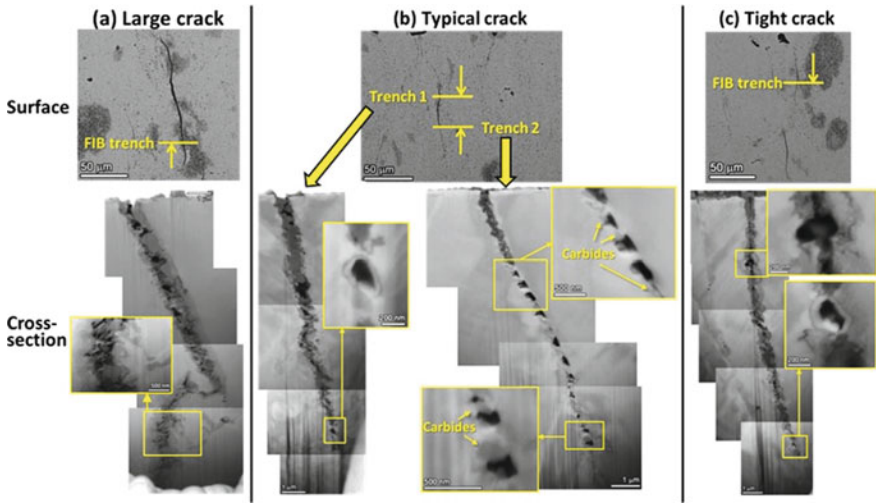


Fig. 11 SEM-BSE images of the morphology of cracks in cross-sections created by FIB in the 1 μm finish, 31% CF Sumitomo CRDM specimen IN033

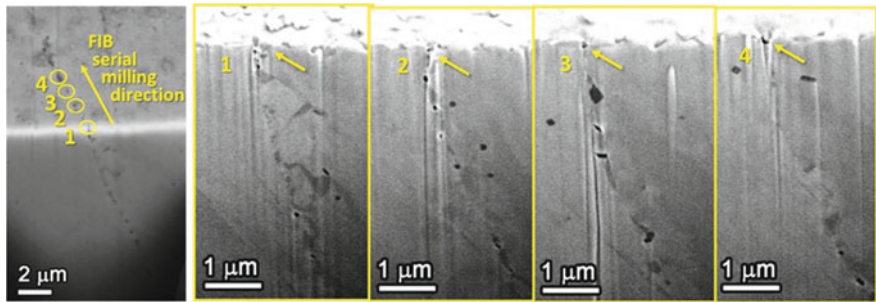


Fig. 12 Low-kV FIB-SE image of surface cavities revealed by serial FIB trenching in the 1 μm finish, 21% CF Sumitomo specimen IN024

cavities that extend to the surface. Therefore, the “postage stamp” surface damage appears to be formed by GB cavities reaching the surface. A qualitative summary on the distribution of the surface GB cavities and IG cracks on the gauge surface of the 12 specimens is provided in Table 4 based on these surface examinations.

Table 4 Qualitative summary of SEM examinations on GB carbides and GB damages

Material, condition	GB carbide distribution		SEM surface observation			SEM cross-section observation	
	Spacing	Size	Spec ID	IG crack	Surface IG cavities	Spec ID	New GB cavities ^a
Sumitomo CRDM, TT + 31% CF	~ 100 nm	Small	IN033	Many	Many	IN034	Many
Sumitomo CRDM, TT + 21% CF	~ 100 nm	Small	IN024	Few	Many	IN026	Some
Valinox CRDM, TT + 31% CF	~ 100 nm	Small	IN036	None	Many	IN038	Very few
Valinox CRDM, TT + 21% CF	~ 100 nm	Small	IN027	None	None	IN029	Some
Valinox CRDM, TT + 12% CF	~ 100 nm	Small	IN065	None	Some	IN067	Very few
Doosan CRDM, TT + 31% CF	~ 0.5–2 μm	Large	IN039	Few	Many	IN041	Some
Doosan CRDM, TT + 21% CF	~ 0.5–2 μm	Large	IN030	None	Many	IN032	Some
TK-VDM plate, TT + 32% CF	~ 100–500 nm	Medium	IN042	Few	Many	IN044	Some
TK-VDM plate, TT + 21% CR	~ 100–500 nm	Medium	IN059	None	Many	IN061	Very few
ANL flat bar, MA + 26% CR	~ 0.2–2 μm	Large	IN053	Few TG cracks	Some	IN055	None
GE B25 K bar, MA + 18% CF	Few IG carbides		IN056	None	None	IN058	None
GE B25 K bar, MA + 12% CF	Few IG carbides		IN062	None	None	IN064	None

^aThe number of new GB cavities is determined by qualitatively comparing the GB cavity distribution at multiple locations in the gauge to that in the shoulder in the cross-section of the same specimen with examples shown in Figs. 16 and 17. Comparison between gauge and shoulder was not made in the specimens where the corresponding cells are left blank

Cross-Section Examination of GB Damage

GB Cavity Morphology in CLT Specimen Cross-Sections

Thirteen specimens were cross-sectioned including 12 ground specimens from every combination of material and cold work condition, as well as the 1 μm finish 31% CF Sumitomo CRDM specimen IN033 that showed the most extensive IG cracks on the gauge surface. The uses are three-fold. Firstly, it enabled a thorough examination relating IG cracks on the surface with their sub-surface morphology in the highly polished specimen IN033. The results revealed a direct correlation between the IG cracks and near-surface GB cavities as shown in Fig. 13. The obvious cracks on the surface usually have an oxidation depth to tens of micrometers with high density of GB cavities ahead of the oxidation front (Fig. 13b). For the possible cracks that haven't opened up on the surface yet, a minimal oxidation depth (<100 nm) is often observed, followed by a series of GB cavities (Fig. 13a). Secondly, the distribution and morphology of GB cavities were evaluated in the entire gauge section for every cross-sectioned specimen. An example is provided in Fig. 14 comparing the GB cavity distribution in the 31 and 21% CF Sumitomo CRDM ground specimens IN034 and IN026 where aggregations of GB cavities that can be easily identified in the low magnification montage images were highlighted in yellow, while sporadically distributed (more discrete) cavities are not marked. The fact that most of the GB cavities were observed on GBs aligned quasi-perpendicular to the loading direction in the cross-section suggested that applied stress played an important role in GB cavity evolution. These aggregations of GB cavities were found to spread randomly through the entire gauge section in both specimens as shown in the montage images in Fig. 14. Meanwhile two images, one taken near the surface and one near the center in the

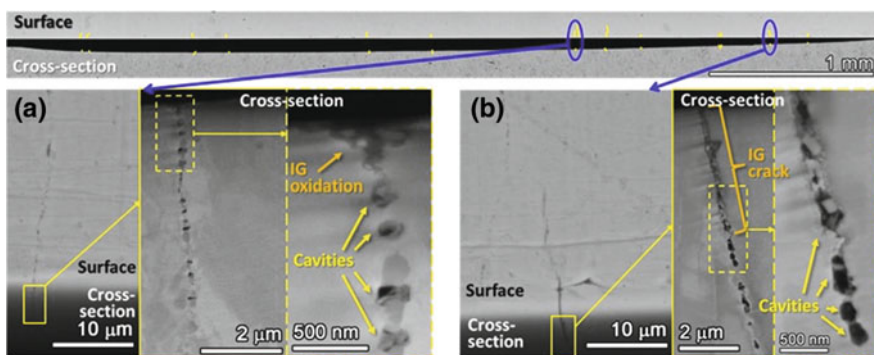


Fig. 13 Comparison of the position of IG cracks identified on the surface and the GB cavities identified in cross-sections in the 31% CF Sumitomo CRDM specimen IN033, accompanied with high-resolution SEM-BSE images highlighting the damage morphology below the identified IG cracks

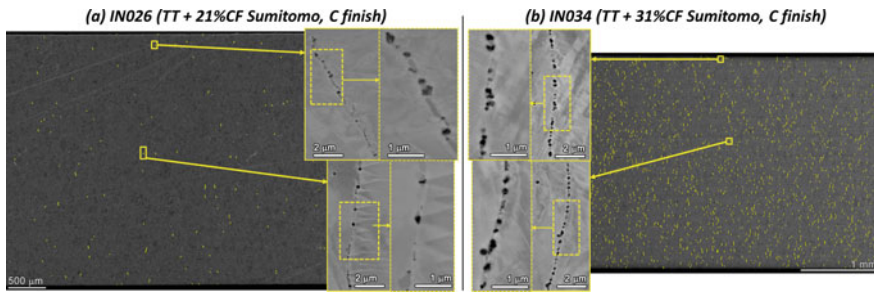


Fig. 14 SEM-BSE montage images of series of GB cavities identified (highlighted in yellow) in the cross-sections of **a** IN026 (21% CF, C finish) and **b** IN034 (31% CF, C finish) from the Sumitomo CRDM heat (Color figure online)

cross-section, were compared for each specimen suggesting similar morphology of GB cavities irrespective of location inside the specimen. However, the density decreased dramatically as the cold work level drops from 31 to 21% CF and the applied stress from 710 to 590 MPa. A similar trend was found in the other heats with examples of GB cavities in the gauge section shown in Fig. 15. The images are displayed at the same scale to facilitate comparison. The GB cavities were very difficult to find in the lower CW specimens, especially those at $\sim 10\%$ CW conditions. It appears that the morphology and density of GB cavities in these specimens did not change significantly from the permanent damage induced by cold work prior to the test despite of the additional ~ 7110 h of exposure at YS. Finally, a comparison in GB cavity distribution was made between gauge section and shoulder in the cross-sections of the $\sim 30\%$ CW specimens. The shoulder section has a much larger diameter where the applied stress is only about $\sim 15\%$ of the YS of the material. As shown in Fig. 16, part of the shoulder was montaged in selected specimens and aggregations of GB cavities were again mapped in the same way as done in Fig. 14. The morphology of GB cavities was also observed at higher magnifications at multiple random sites in the shoulder and compared to that in the gauge section. In Fig. 17, the typical morphology of GB cavities in the gauge (upper row) is compared to that in the shoulder (lower row) in the highly CW specimens from different heats. An obvious increase in the size and density of GB cavities was observed in the 31% CF materials with small but semi-continuous distribution of GB carbides, while no apparent changes was found in the TT + 31% CF Doosan CRDM heat or the MA + 26% CR ANL bar heat featuring large and spaced carbides at GBs (Figs. 16 and 17). A brief summary of the cross-section examination is also given in Table 4 with more details to be found in [16].

GB Cavity Quantification

More detailed analyses have been completed for the 31% CF Valinox CRDM specimen IN038 and the 31% CF Doosan CRDM specimen IN041 in which the size

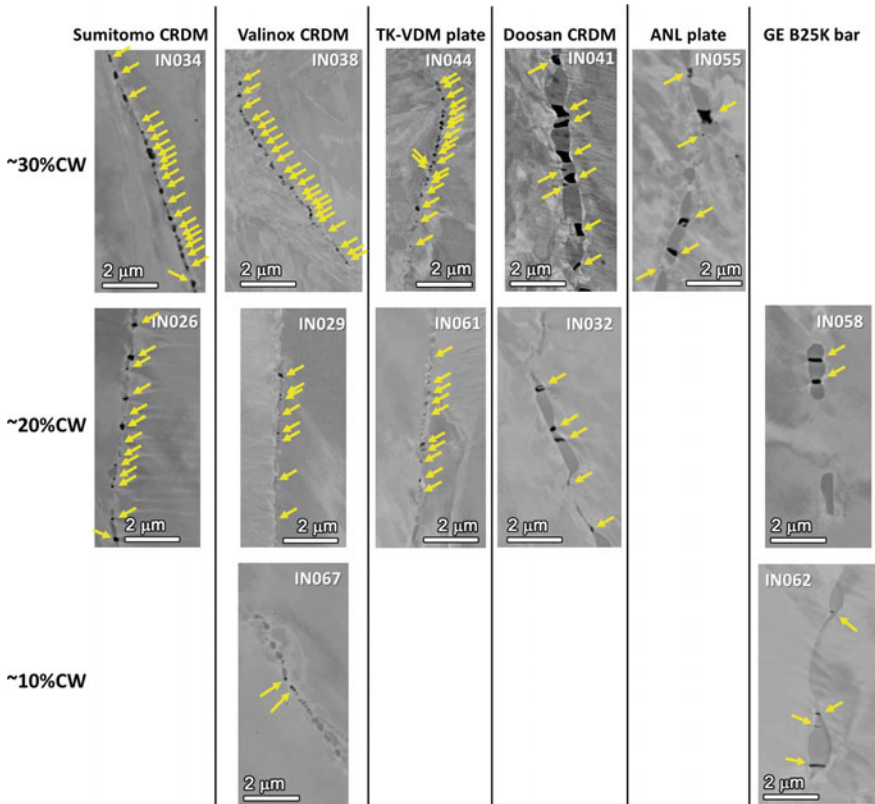


Fig. 15 SEM-BSE images of the typical morphology of high-density cavity region in the gauge cross-section of the ground specimens after 9220 (IN034, IN038, IN044, IN041, IN026, IN029, IN032) or 7110 (IN055, IN058, IN067, IN062) hours of exposure. The specimens are grouped by cold work levels and the images are displayed at the same magnification to facilitate comparison. GB cavities are highlighted by arrows

and spacing of GB carbides are significantly different as summarized in Table 2. For each specimen, the number and size of GB cavities were measured in a $150 \times 150 \mu\text{m}$ area at locations corresponding to 15, 50, 70, 85 and 100% YS for each specimen. Since the number of grains and the total length of GBs examined in the $150 \times 150 \mu\text{m}$ area vary at different locations and among specimens, the GB cavity distribution is evaluated per unit GB length instead of per unit surface area examined. Several specific aspects are determined to help quantify the observed cavities: (a) number of cavities per unit GB length (= total number of cavities observed/total length of examined GBs); (b) average distance between cavities (= total length of examined GBs/total number of cavities observed) and (c) cavity surface area per unit GB length (= total cross-sectional area occupied by cavities/total length of examined GBs). As shown in Fig. 18a, a higher applied stress (>70% YS) resulted in a sharp increase in the number of cavities for the 31%

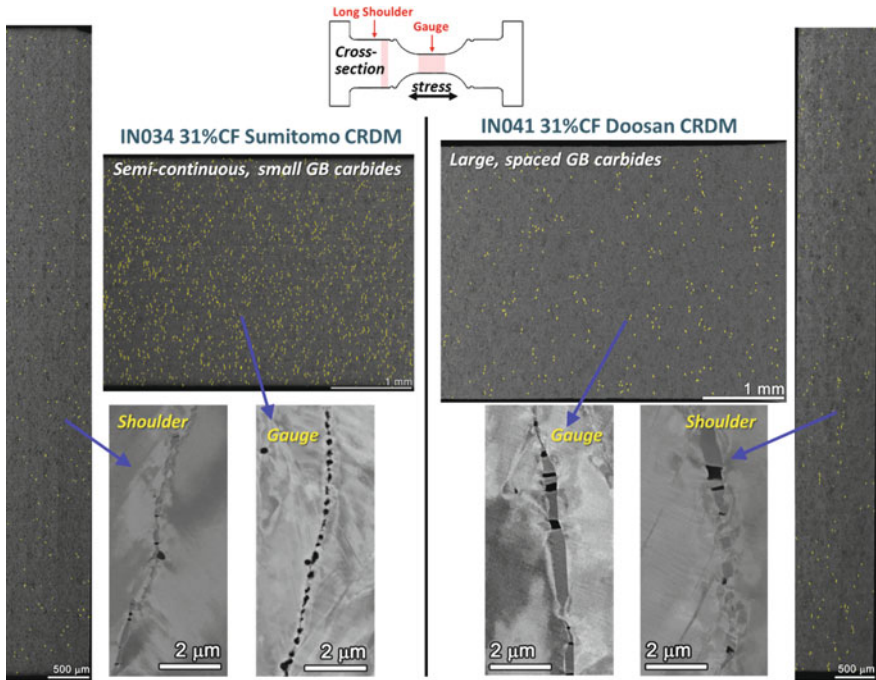


Fig. 16 SEM-BSE montage images of series of GB cavities (highlighted in yellow) identified in the cross-sections of the gauge and the long shoulder in the Sumitomo CRDM specimen IN034 (TT + 31% CF, C finish) and the Doosan CRDM specimen IN041 (TT + 31% CF, C finish). Higher magnification BSE images on GB cavities in the gauge and the shoulder are also shown (Color figure online)

CF Valinox CRDM specimen IN038. This clearly suggests that new cavity nucleation sites were created during the constant load test beyond the preexisting damage due to cold work. In contrast, the 31% CF Doosan CRDM specimen IN041 only showed a limited increase in the number of cavities and revealed very little change even at higher applied stress. Another way of looking at the same set of data is through the average distance between cavities (Fig. 18b) where a decrease in the distance between cavities was observed in the Valinox specimen IN038 at high applied stress. The estimated average distance between cavities dropped from $\sim 2 \mu\text{m}$ at low stress locations (15–50% YS) to below $1 \mu\text{m}$ at 100% YS, consistent with the semi-continuous distribution of GB cavities found in the gauge of this specimen as shown in Figs. 14–17. In comparison, the average distance between cavities in IN041 may decrease slightly from ~ 2.8 to $\sim 2.3 \mu\text{m}$, but the cavity spacing remains much larger than that in IN038. This is also consistent with the observation of the larger spacing between GB carbides in this material, which is $\sim 1\text{--}5 \mu\text{m}$ apart (Table 2). Interestingly, the cross-sectional area occupied by cavities area per unit GB length in IN041 is higher as compared to IN038 (Fig. 18c), but this is due to the much larger preexisting cavities induced by cold

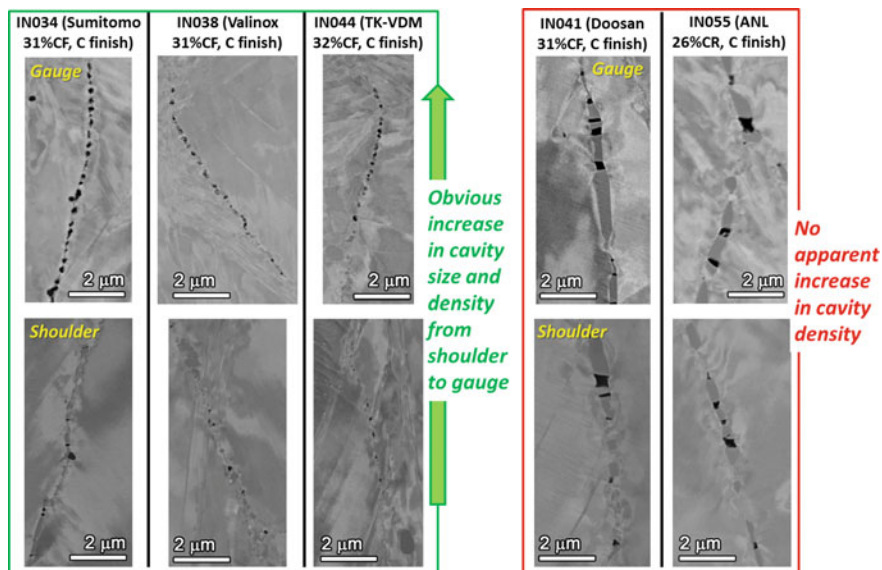


Fig. 17 SEM-BSE images on the typical morphology of GB cavities observed in the high-stress gauge (upper row) versus the low-stress shoulder (lower row) in the $\sim 30\%$ CW specimen from five different heats

work associated with the larger carbides in the Doosan material. With the increase in applied stress from 50 to 100% YS, the cavity area per unit GB length the Valinox IN038 specimen increased by $\sim 2.5X$, while Doosan IN041 changes only a small amount. This again reflects the nucleation and faster growth of GB cavities in IN038 at high applied stress. These quantitative results provide complimentary information to the qualitative SEM examinations. It confirmed that a highly CW alloy 690 material with a semi-continuous distribution of small GB carbides and limited preexisting damage is susceptible to cavity nucleation and growth at high stress in 360 °C PWR primary water. In contrast, a highly CW alloy 690 material with larger, well-spaced carbides and more extensive preexisting damage are more resistance to GB cavity formation and growth.

Discussion

This study represents the first-ever observation of IG crack nucleation for alloy 690 in PWR primary water under constant load conditions. Different from the classical notion of SCC initiation, the SCC initiation in highly CW alloy 690 in this test is directly associated with small, closely spaced GB cavities reaching the surface and converting into short cracks. Comparisons between surface observations of IG cracks and cross-section observation of GB cavities revealed that the density of

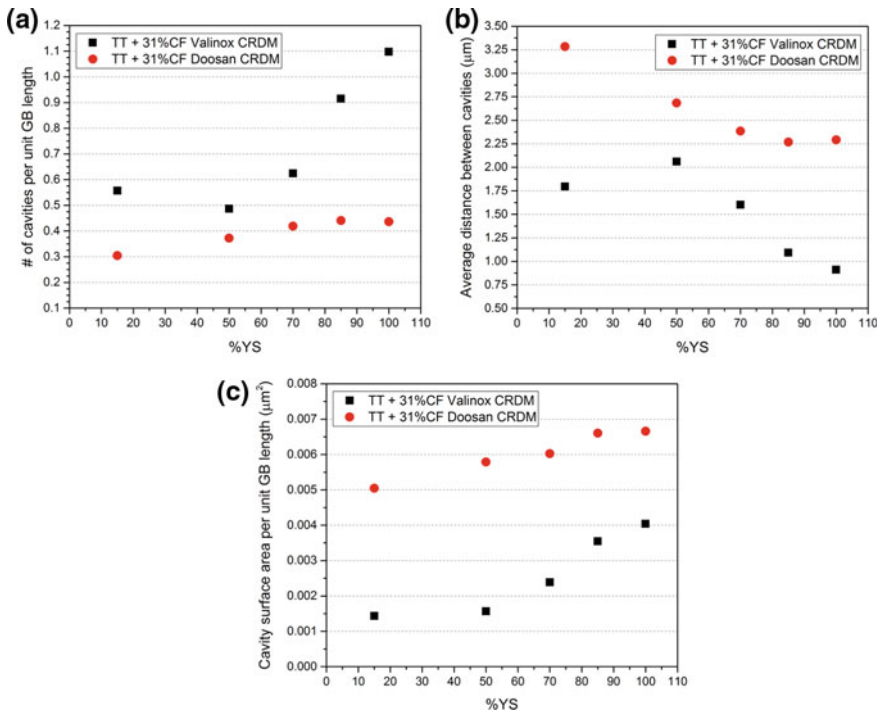


Fig. 18 Density and size of cavities interpreted by **a** number of cavities per unit GB length, **b** average distance between GB cavities and **c** total cross-sectional surface area of cavities per unit GB length as a function of % YS in the 31% CF Valinox CRDM alloy 690TT specimen IN038 and Doosan CRDM alloy 690TT specimen IN041

surface cracks scaled with density of GB cavities inside the material. The facts that these cavities were distributed across the entire gauge section (Fig. 14) and decreased with decreasing applied stress (Fig. 18) suggests that this process is creep dominated. While creep cavities have already been evidenced after dynamic straining using slow cyclic loading ramps [13] and in pre-cracked or blunt notch CT specimens under a stress gradient in front of crack tips [12, 14, 20], the latest results demonstrate that creep strain rates produced under constant load are sufficient to promote GB cavity formation and growth in CW alloy 690 in 360 °C PWR primary water. However, the GB cavity distribution differs among the alloy 690 heats and varies with cold work and applied stress. Below a more detailed discussion is provided on the effect of these influencing factors on cavity evolution in CW alloy 690.

Effect of Cold Work and Applied Stress on GB Cavity Evolution

The various cold work levels prepared for different heats in the specimen matrix enabled a correlation between SCC initiation susceptibility and cold work. As shown in Figs. 14 and 15 and as summarized in Table 4, cold work clearly promoted IG crack nucleation under constant load in this study. This can be attributed to the role of cold work and a high applied stress on both nucleation and growth of GB cavities. As shown in Fig. 2, pre-test cold working induced a low density of small cavities at carbide-matrix interfaces and cracked carbides. Since the degree of this pre-existing damage scales with cold work, more cavity nucleation sites are readily available in materials with higher cold work level. They also act as stress concentrators that facilitate vacancy condensation, leading to subsequent cavity growth. Secondly, it is known that higher plastic strain induces more vacancies in materials [21] and Arioka et al. [14] attributed the higher density of GB cavities in highly CW materials to a larger amount of athermal vacancies produced by cold work. However, it should be noted that the applied stress for all initiation specimens was equivalent to the CW material yield stress therefore roughly scaled with the degree of cold work. The higher applied stress in highly CW materials likely resulted in a higher creep strain as partially reflected in the DCPD-indicated non-referenced strain in Fig. 7. Increase in applied stress may have generated more vacancies through work hardening and dislocation pile-ups at carbide interfaces. Along with vacancy diffusion, the dislocation creep induced by applied stress can also contribute to higher cavity coverage at GBs. In addition, important insights were gained from cavity quantification in selected specimens. As shown in Fig. 18, the effect of applied stress on cavity distribution has a strong dependence on starting GB microstructure. When subjected to susceptible microstructure (i.e. the semi-continuous distribution of small carbides on GBs), the GB cavity distribution sharply increased at an applied stress >70% YS in the highly CW Valinox CRDM specimen IN038, and the density and size of cavities doubled from 50 to 100% YS. This clearly demonstrates that increasing applied stress can promote both cavity nucleation and growth, especially when it is higher than 70% YS. However, the increase of applied stress had little effect on cavity evolution in the 31% CF Doosan CRDM specimen IN041 featuring large and widely spaced carbides.

Effect of Starting Microstructure on GB Cavity Evolution

As mentioned above, the starting GB carbide microstructure also plays an important role in cavity evolution in CW alloy 690. Although GB carbides are generally considered beneficial to IGSCC resistance in alloy 600, they acted as nucleation sites for cavities in this study. This is consistent with the belief that GB cavities are formed at geometrical or structural irregularities where high stress concentrations

develop [22]. In previous studies, Arioka et al. [12, 14] suggested that the stress concentrations at GB carbides promote condensation of excess vacancies from cold work to form small IG cavities, reduce GB cohesive strength and eventually lead to crack initiation and growth. Interestingly, the alloy 690TT CRDM tubing that is commonly considered to have an optimized microstructure (very homogeneous grain structures and semi-continuous distributions of small GB carbides with no significant compositional banding) turned out to be the most susceptible to cavity evolution among the heats evaluated in this study. As shown in Fig. 15, the size, shape and spacing of GB cavities appear to directly depend on the distribution of IG carbides. For the two alloy 690TT CRDM heats (Sumitomo and Valinox) and the alloy 690TT TK-VDM plate heat which feature a semi-continuous distribution of small (<300 nm in size) IG carbides, a high density of small GB cavities were produced during testing of the 31% CF specimens. GB cavities in the 31% CF specimens in these heats are seen to produce a semi-continuous distribution that begin to link up and form IG cracks as the test time progresses. The Doosan alloy 690TT CRDM and the ANL alloy 690 MA bar were quite different with GB carbides that are larger, more elongated, blocky and well-spaced, creating a lower density of cavities that are larger, faceted and more isolated. Even though the cavities in the highly CW and highly stressed specimens with this type of microstructure can be 2–5 times larger, a semi-continuous distribution of cavities do not form that can link up and induce IG crack nucleation. Figure 17 highlights the heat-to-heat comparison documenting cavity distributions for the highly CW materials in the high-stress gauge section versus the low-stress shoulder region. For the materials exhibiting semi-continuous small GB carbides, the size and density of cavities in the gauge of the highly CW specimens are remarkably higher after testing than those in the shoulder. In contrast, no or little increase was observed in the cavity distribution between the gauge and the shoulder in the materials with large and more widely spaced carbides despite of the high CW and high stress level in the specimen. This trend was further confirmed by cavity quantification shown in Fig. 18 where for the 31% CF Valinox CRDM specimen IN038 exhibits a much higher density of cavities at high stress in comparison to those in the 31% CF Doosan CRDM specimen IN041.

Currently the test has been restarted on remaining specimens. The specimens removed for destructive examination were replaced with new CW specimens selected to evaluate the effects of grain boundary carbides (comparing thermally treated versus solution annealed materials) and applied stress (comparing response at 90% YS to that at 100% YS) on IG cavity formation and the nucleation of small cracks. In addition, another highly CW plate heat that exhibited a relatively low SCC growth rate was added for evaluation of its SCC initiation susceptibility. The plan is to stop the test when the replacement specimens reach ~1 year of exposure (matching previous specimens discussed above) and the original specimens reach ~2 years of exposure to again document the damage evolution on specimen surfaces. Based on these results, selected specimens may be removed for destructive examinations to help quantify the evolution of SCC initiation precursors.

Conclusion

Long-term constant load SCC initiation testing has been performed in simulated PWR primary water on six commercial alloy 690 heats at various cold work levels. This paper reviews the testing and microstructural characterization results at the first test interruption after ~ 1 year of exposure with key information below:

- IG crack nucleation has been observed for the first time in highly CW alloy 690 specimens under constant load in 360 °C PWR primary water. The mechanism differs from classical SCC initiation and occurs due to formation of nano-size, closely spaced GB cavities intersecting the surface.
- GB cavity formation and growth is a result of creep deformation and is strongly influenced by the material microstructure, the degree of cold work and the applied stress. Increasing GB coverage of small-size carbides, cold work level and applied stress have all been shown to enhance IG damage during SCC initiation testing. The thermally treated microstructure (high GB carbide coverage) appears to be most sensitive to this precursor damage evolution when cold worked to levels $\geq 20\%$.

Acknowledgements The authors gratefully acknowledge the financial support from the Office of Nuclear Energy, U.S. Department of Energy through the Light Water Reactor Sustainability Program. In addition, support is recognized from the U.S. Nuclear Regulatory Commission for SCC crack growth rate testing and pre-test microstructural characterizations of the CW materials and from the Office of Basic Energy Sciences, U.S. Department of Energy for high-resolution grain boundary examinations. Key experimental support was provided by Dr. John Deibler at PNNL for conducting the finite element modeling. Key technical assistance from Robert Seffens, Clyde Chamberlin, Anthony Guzman and Ryan Bouffloux is acknowledged for SCC initiation testing and materials preparation activities.

References

1. D.J. Paraventi, W.C. Moshier, Alloy 690 SCC growth rate testing, in *Workshop on Cold Work in Iron- and Nickel-Base Alloys* (EPRI, 2007)
2. P.L. Andresen, M.M. Morra, J. Hickling, A. Ahluwalia, J. Wilson, Effect of deformation and orientation on SCC of alloy 690, in *14th International Conference on Environmental Degradation of Materials in Nuclear Power Systems—Water Reactors* (American Nuclear Society, 2009), p. 846
3. D.R. Tice, S.L. Medway, N. Platts, J.W. Startmand, Crack growth testing on cold worked alloy 690 in primary water environment, in *15th International Conference on Environmental Degradation of Materials in Nuclear Power Systems—Water Reactors* (The Minerals, Metals & Materials Society, 2011), p. 71
4. S.M. Bruemmer, M.J. Olszta, N.R. Overman, M.B. Toloczko, Cold work effects on stress corrosion crack growth in alloy 690 tubing and plate materials, in *17th International Conference on Environmental Degradation of Materials in Nuclear Power Systems—Water Reactors* (Canadian Nuclear Society, 2015)

5. M.B. Toloczko, S.M. Bruemmer, Crack growth response of alloy 690 in simulated PWR primary water, in *14th International Conference on Environmental Degradation of Materials in Nuclear Power Systems—Water Reactors* (American Nuclear Society, 2009), p. 706
6. M.B. Toloczko, S.M. Bruemmer, Cold rolling effects on stress corrosion crack growth in alloy 690 tubing and plate materials, in *15th International Conference on Environmental Degradation of Materials in Nuclear Power Systems—Water Reactors* (The Minerals, Metals & Materials Society, 2011), p. 91
7. R.H. Jones, S. Bruemmer, Environment-induced crack growth processes in nickel-base alloys, in *1st International Conference on Environment-Induced Cracking of Metals* (1988), p. 287
8. G.S. Was, Grain-boundary chemistry and intergranular fracture in austenitic nickel-base alloys—A review. *Corrosion* (Houston) **46**, 319–330 (1990)
9. P. Andresen, M.M. Morra, A. Ahluwalia, Effect of deformation temperature, orientation and carbides on SCC of alloy 690, in *16th International Conference on Environmental Degradation of Materials in Nuclear Power Systems—Water Reactors* (NACE International, 2013)
10. K. Arioka, T. Yamada, T. Terachi, G. Chiba, Influence of carbide precipitation and rolling direction on intergranular stress corrosion cracking of austenitic stainless steels in hydrogenated high-temperature water. *Corrosion* (Houston) **62**, 568–575 (2006)
11. S.M. Bruemmer, M.J. Olszta, N.R. Overman, M.B. Toloczko, Microstructural effects on stress corrosion cracking of cold-worked alloy 690 tubing and plate materials, in *16th International Conference on Environmental Degradation of Materials in Nuclear Power Systems—Water Reactors* (NACE International, 2013)
12. K. Arioka, R.W. Staehle, T. Yamada, T. Miyamoto, T. Terachi, Degradation of alloy 690 after relatively short times. *Corrosion* (Houston) **72**, 1252–1268 (2016)
13. Z. Zhai, M.B. Toloczko, K. Kruska, S. Bruemmer, Precursor evolution and SCC initiation of cold-worked alloy 690 in simulated PWR primary water. *Corrosion* (Houston), (2017) (under review)
14. K. Arioka, Whitney award lecture: Change in bonding strength at grain boundaries before long term SCC initiation. *Corrosion* (Houston) **71**(2015), 403–419 (2014)
15. M.B. Toloczko, N.R. Overman, M.J. Olszta, S.M. Bruemmer, Pacific Northwest National Laboratory investigation of stress corrosion cracking in nickel-base alloys, in *Stress Corrosion Cracking of Cold-Worked Alloy 690*, NUREG/CR-7103 vol. 3 (Nuclear Regulatory Commission, Office of Nuclear Regulatory Research, 2015)
16. Z. Zhai, M.B. Toloczko, K. Kruska, D.K. Schreiber, M.J. Olszta, N.R. Overman, S. Bruemmer, *Precursor damage evolution and stress corrosion crack initiation of cold-worked alloy 690 in PWR primary water*. Pacific Northwest National Laboratory: Technical Milestone Report M2LW-16OR0402034, Light Water Reactor Sustainability Program, DOE Office of Nuclear Energy, Sept 2016
17. S.M. Bruemmer, M.J. Olszta, D.K. Schreiber, M.B. Toloczko, *Corrosion and stress corrosion crack initiation of cold worked alloy 600 and alloy 690 in PWR primary water environments*. Pacific Northwest National Laboratory: Technical Milestone Report M2LW-13OR0402035, Light Water Reactor Sustainability Program, DOE Office of Nuclear Energy, Sept 2014
18. Z. Zhai, M.J. Olszta, M.B. Toloczko, S.M. Bruemmer, Precursor corrosion damage and stress corrosion crack initiation in alloy 600 during exposure to PWR primary water, in *17th International Conference on Environmental Degradation of Materials in Nuclear Power Systems—Water Reactors* (Canadian Nuclear Society, 2015)
19. K. Kruska, Z. Zhai, M.B. Toloczko, S. Bruemmer, Characterization of SCC initiation precursors in cold-worked alloy 690, in *CORROSION 2017*, NACE (2017)
20. K. Arioka, T. Yamada, T. Miyamoto, T. Terachi, Dependence of stress corrosion cracking of alloy 690 on temperature, cold work, and carbide precipitation—role of diffusion of vacancies at crack tips. *Corrosion* (Houston) **67**, 035006-035001–035006-035018 (2011)
21. H.G. Van Bueren, Theory of the formation of lattice defects during plastic strain. *Acta Metall.* **3**, 519–524 (1955)
22. J. Cadek, *Creep in Metallic Materials* (Elsevier, 1988)